



Contents lists available at ScienceDirect

Communications in Nonlinear Science and Numerical Simulation

journal homepage: www.elsevier.com/locate/cnsns

Research paper

Efficient manipulation of Bose–Einstein Condensates in a double-well potential

Jimmie Adriaola^{a,*}, Roy Goodman^a, Panayotis Kevrekidis^b^a Department of Mathematical Sciences, New Jersey Institute of Technology, University Heights, 07102, Newark, USA^b Department of Mathematics and Statistics, University of Massachusetts Amherst, 01003-4515, Amherst, USA

ARTICLE INFO

Article history:

Received 14 June 2022

Received in revised form 7 January 2023

Accepted 8 March 2023

Available online 12 March 2023

Keywords:

Quantum control

Hamiltonian dynamical systems

Galerkin methods

ABSTRACT

We pose the problem of transferring a Bose–Einstein Condensate (BEC) from one side of a double-well potential to the other as an optimal control problem for determining the time-dependent form of the potential. We derive a reduced dynamical system using a Galerkin truncation onto a finite set of eigenfunctions and find that including *three* modes suffices to effectively control the full dynamics, described by the Gross–Pitaevskii model of BEC. The functional form of the control is reduced to finite dimensions by using another Galerkin-type method called the chopped random basis (CRAB) method, which is then optimized by a genetic algorithm called differential evolution (DE). Finally, we discuss the extent to which the reduction-based optimal control strategy can be refined by means of including more modes in the Galerkin reduction.

Published by Elsevier B.V.

1. Introduction

The dynamics of solitary waves in dispersive media with external potentials is a topic of widespread scientific interest, as it arises in many areas of application. For instance, in Bose–Einstein Condensates (BEC) of, e.g., alkali gases, external potentials may be created using a variety of physical mechanisms including optical and magnetic fields, and may consist of one or a few wells or a periodic array, and may effectively confine the BEC to one, two, or three space dimensions [1–4]. Another appealing experimental setting is the nonlinear propagation of light through photonic crystals, and in the quasi-discrete realm of optical waveguides [5,6]. Here, a spatially-dependent index of refraction induces an effective potential [7].

In both these applications, the simplest potential enabling bifurcation phenomena and nontrivial dynamics is arguably the double well potential. It has been studied intensely in the atomic realm, following the hallmark theoretical work of [8]. These predicted Josephson oscillations between the wells and quantum self-trapping were subsequently realized experimentally in [9], as well as a dynamical symmetry-breaking bifurcation later observed in [10]. More recent experiments have added damping and driving, which may present novel phenomena including stochastic resonance [11]. Relevant double-well experiments have been conducted in the optical setting as well. The work of [12] considered the double-well potential in the context of twin-core self-guided laser beams in Kerr media, while [13] probed two-well dynamics using photorefractive crystals. In this latter setting, additional phenomena were demonstrated in a *triple-well* potential [14].

Naturally, this large volume of experimental developments and control has motivated a wide range of theoretical explorations in numerous further directions. The relevant list is too long to do it proper justice, but we mention some

* Correspondence to: University of California, Santa Barbara, USA.
E-mail address: jadriazola@ucsb.edu (J. Adriaola).

related studies. Some more mathematical examples include the analysis of the double-well bifurcation structure [15,16], the low-dimensional representation of the associated dynamical problem (and its fidelity) [17,18], and the effect of changing the nonlinear exponent on the bifurcation [19,20]. Physical examples include the interactions of multiple dispersive (e.g., atomic) species [21–23], incorporating beyond-mean-field (i.e., many-body) effects [24,25], and the effect of larger spatial dimensions (and possibly four wells) [26], among others.

In this work, we apply ideas from nonlinear dynamics to simplify and gain intuition into an optimal control problem of manipulating BEC [27,28]. Optimal control methodology has long been recognized as a versatile tool for engineering on-demand quantum states of interest. In the early stages, magnetic microtraps controllable by external parameters including radio-frequency fields or/and wire currents were used to enable the preparation of desired states [29]—see also the detailed analysis of the relevant methodologies and their numerical MATLAB-based implementation in [30,31]. Subsequent work, including [32], applied these ideas in fully three-dimensional settings. More recently, two of the present authors have used these ideas to re-shape the density distribution of an atomic BEC and alter the topology of its support [33].

Here, more concretely, we apply low-dimensional approximations commonly used to study the dynamics of confined dispersive waves (as in, e.g., [26,34]) as a basis for the optimal transfer of a BEC between the two wells of a potential. The calculated control policy is then applied to both the low-dimensional setting and to the full mean-field model described by the Gross-Pitaevskii equation, a nonlinear Schrödinger partial differential equation (PDE) with a potential [3,4]. Along the way, we learn the following lesson, which we find interesting and important. The two-mode expansion is commonly used to study the double-well system and is widely acknowledged to describe the dynamics, both qualitatively and even quantitatively. By contrast, we find that this optimal control problem requires at least a three-mode approximation to achieve useful agreement. We believe that such lessons may prove useful in related contexts.

Our presentation is structured as follows. In Section 2, we present the physical and mathematical setup and its reduced (two- and three-mode) representation. Subsequently, in Section 3, we present the proposed optimal control strategy. In Section 4, we display numerical results. Finally, Section 5 provides a summary of our conclusions, as well as a number of directions for future study.

2. Derivation of reduced model systems

The approach to optimization we propose here is to apply optimal control to a finite-dimensional model system, whose derivation we outline in this section. In particular, we use Galerkin truncation to derive a low-dimensional Hamiltonian system whose dynamics capture the essence of the full dynamics. The latter, in turn, is described by a Gross-Pitaevskii equation (GPE) in one spatial dimension. This system may be derived from a three-dimensional model in the presence of an anisotropic potential that squeezes the condensate into an effectively one-dimensional arrangement; see details and nondimensionalization, e.g., in [1]. The initial and (final) desired conditions used throughout are set to the stable fixed points of the finite-dimensional model Hamiltonian we have derived. These fixed points correspond to the two asymmetric states which exist in the presence of the barrier. Indeed, our aim is to drive the atomic mass from a state predominantly localized in one well to a state localized in the other. The efficiency will be determined on the basis of how successful such a transfer is with an appropriate definition of “fidelity” to the intended end state; more detail will follow the analysis.

The GPE model is a nonlinear Schrödinger equation with a spatial potential

$$i\partial_t \psi = \mathcal{L}(x, \mathbf{w}(t)) \psi + \mathcal{N}(\psi) = -\frac{1}{2} \partial_x^2 \psi + V(x, \mathbf{w}(t)) \psi + |\psi|^2 \psi, \tag{2.1}$$

where $\mathbf{w}(t)$ is a time-dependent vector of C^0 control functions. In addition to conserving a Hamiltonian energy, this system conserves the mass

$$M = \int_{-\infty}^{\infty} |\psi|^2 dx, \tag{2.2}$$

which in the BEC context is interpreted as the total number of atoms in the condensate. The potential V is chosen as the superposition of a quadratic confining potential, usually implemented via magnetic fields [3,4], and a thin, tall barrier at the center, typically induced by an optical beam [10]. Added together, these form a prototypical double-well potential; see, also, [35]. In particular, the potential takes the form

$$V = \frac{1}{2} u(t) x^2 + v(t) \delta(x), \tag{2.3}$$

where the first term models the magnetic confinement and the second term models the localized repulsive barrier at the center, as we assume $v(t) > 0$. The time-dependent parameter vector is thus given by $\mathbf{w}(t) = (u(t), v(t))^T$.

Let $\Phi_{\mathbf{w}} = \{ \varphi_n(x; \mathbf{w}) \in L^2(\mathbb{R}) \mid n = 0, 1, \dots \}$ be the set of normalized eigenfunctions of the linear Schrödinger eigenvalue problem

$$\mathcal{L}(x, \mathbf{w}) \varphi_n = E_n \varphi_n, \tag{2.4}$$

for a fixed parameter vector \mathbf{w} . Because $\Phi_{\mathbf{w}}$ is complete in $L^2(\mathbb{R})$, we may represent the solution to Eq. (2.1) at time t by the infinite series

$$\psi(x, t) = \sum_{n=0}^{\infty} c_n(t) \varphi_n(x; \mathbf{w}(t)).$$

Plugging this representation into Eq. (2.1), and projecting both sides of the equation onto φ_n – in the $L^2(\mathbb{C})$ sense – yields an evolution equation for $c_n(t)$. Together, the evolution of the infinite vector $\mathbf{c} = (c_0(t), c_1(t), \dots)$ of complex amplitudes is then equivalent to the evolution of ψ under GPE.

To derive an approximate reduced system, we consider the truncated series superposition of instantaneous eigenfunctions

$$\psi_{N+1}^{\text{Gal}} := \sum_{n=0}^N c_n(t) \varphi_n(x; \mathbf{w}(t)) \tag{2.5}$$

for some fixed value of $N < \infty$. Ignoring any truncation error due to the terms in the omitted tail of the series yields the system of interest. Such a truncation has been rigorously justified in certain very simple cases, e.g. [18,36], but the method is commonly applied without rigorous justification.

2.1. Two-mode expansion

By setting $N = 1$ in Expansion (2.5), we find the following two-mode Hamiltonian system [35]:

$$\begin{aligned} i\dot{c}_0 &= \frac{\partial \mathcal{H}}{\partial \bar{c}_0} = \alpha c_0 + \gamma_0 |c_0|^2 c_0 + \gamma_2 (c_1^2 \bar{c}_0 + 2c_0 |c_1|^2), \\ i\dot{c}_1 &= \frac{\partial \mathcal{H}}{\partial \bar{c}_1} = \beta c_1 + \gamma_1 |c_1|^2 c_1 + \gamma_2 (c_0^2 \bar{c}_1 + 2c_1 |c_0|^2), \end{aligned} \tag{2.6}$$

with instantaneous projection coefficients given by

$$\alpha = \langle \mathcal{L}\varphi_0, \varphi_0 \rangle, \quad \beta = \langle \mathcal{L}\varphi_1, \varphi_1 \rangle, \quad \gamma_0 = \|\varphi_0\|^4, \quad \gamma_1 = \|\varphi_1\|^4, \quad \gamma_2 = \langle \varphi_0^2, \varphi_1^2 \rangle. \tag{2.7}$$

Its Hamiltonian reads:

$$\mathcal{H} = \alpha |c_0|^2 + \beta |c_1|^2 + \frac{\gamma_0}{2} |c_0|^4 + \frac{\gamma_1}{2} |c_1|^4 + \gamma_2 (\Re \{c_0^2 \bar{c}_1^2\} + 2|c_0|^2 |c_1|^2). \tag{2.8}$$

This expansion holds under the general assumption that $V(x, \mathbf{w}(t)) = V(-x, \mathbf{w}(t))$, i.e., that the potential is even. This system conserves a discrete form of the mass defined in Eq. (2.2),

$$M_d(t) = |c_0(t)|^2 + |c_1(t)|^2. \tag{2.9}$$

This system has stationary solutions of the form $(c_0(t), c_1(t)) = (\rho_0, \rho_1)e^{-i\Omega t}$. In particular, it has a solution corresponding to the nonlinear continuation of the ground state with $\rho_1 = 0$ and $\Omega = \alpha + \gamma_0 \rho_0^2$, and a second solution corresponding to the nonlinear continuation of the excited state, with $\rho_0 = 0$ and $\Omega = \beta + \gamma_1 \rho_1^2$. In the absence of a barrier, i.e., for $v = 0$, and total mass $M_d = 1$, these are the only such states, and both are linearly stable. In the presence of a barrier, however, the excited state can become unstable in a symmetry-breaking pitchfork bifurcation.

We may take advantage of the conservation law of Eq. (2.9) to reduce the system from two degrees of freedom to one as follows, which provides a convenient visualization of the dynamics and bifurcation. Consider the canonical transformation

$$c_0 = Ae^{i\theta}, \quad c_1 = (q + ip)e^{i\theta}. \tag{2.10}$$

We reduce the number of degrees of freedom from two to one using the conserved mass (2.9) which now reads $A^2 = M_d - q^2 - p^2$. The Hamiltonian in these coordinates is given by

$$\begin{aligned} \mathcal{H} &= \frac{\gamma_0 M_d^2}{2} + \alpha M_d + q^2 (\beta - \alpha + M_d (3\gamma_2 - \gamma_0)) + p^2 (\beta - \alpha + M_d (\gamma_2 - \gamma_0)) \\ &+ \left(\frac{\gamma_0}{2} + \frac{\gamma_1}{2} - \gamma_2\right) p^4 + (\gamma_0 + \gamma_1 - 4\gamma_2) p^2 q^2 + \left(\frac{\gamma_0}{2} + \frac{\gamma_1}{2} - 3\gamma_2\right) q^4. \end{aligned} \tag{2.11}$$

We show the phase portraits associated with Hamiltonian (2.11) for values of $v = 0$ and $v = 10$ with fixed $M_d = 1$ with $u = 1$ in the first column of Fig. 2.1. In the reduced system, the ground state standing wave becomes a fixed point at the origin, and the excited state standing wave becomes the boundary circle $p^2 + q^2 = 1$. For $v = 10$, two new asymmetric states have emerged from the odd solution and appear as fixed points on the q -axis. The right column shows the standing waves constructed from the Galerkin ansatz, including the initial and desired states of the control problem ψ_0 and ψ_d .

For $v = 0$, the double-well structure is absent (i.e., the setting is one of a parabolic trap with equidistant linear eigenvalues), hence the two-mode reduction is not expected to provide an adequate representation of the dynamics

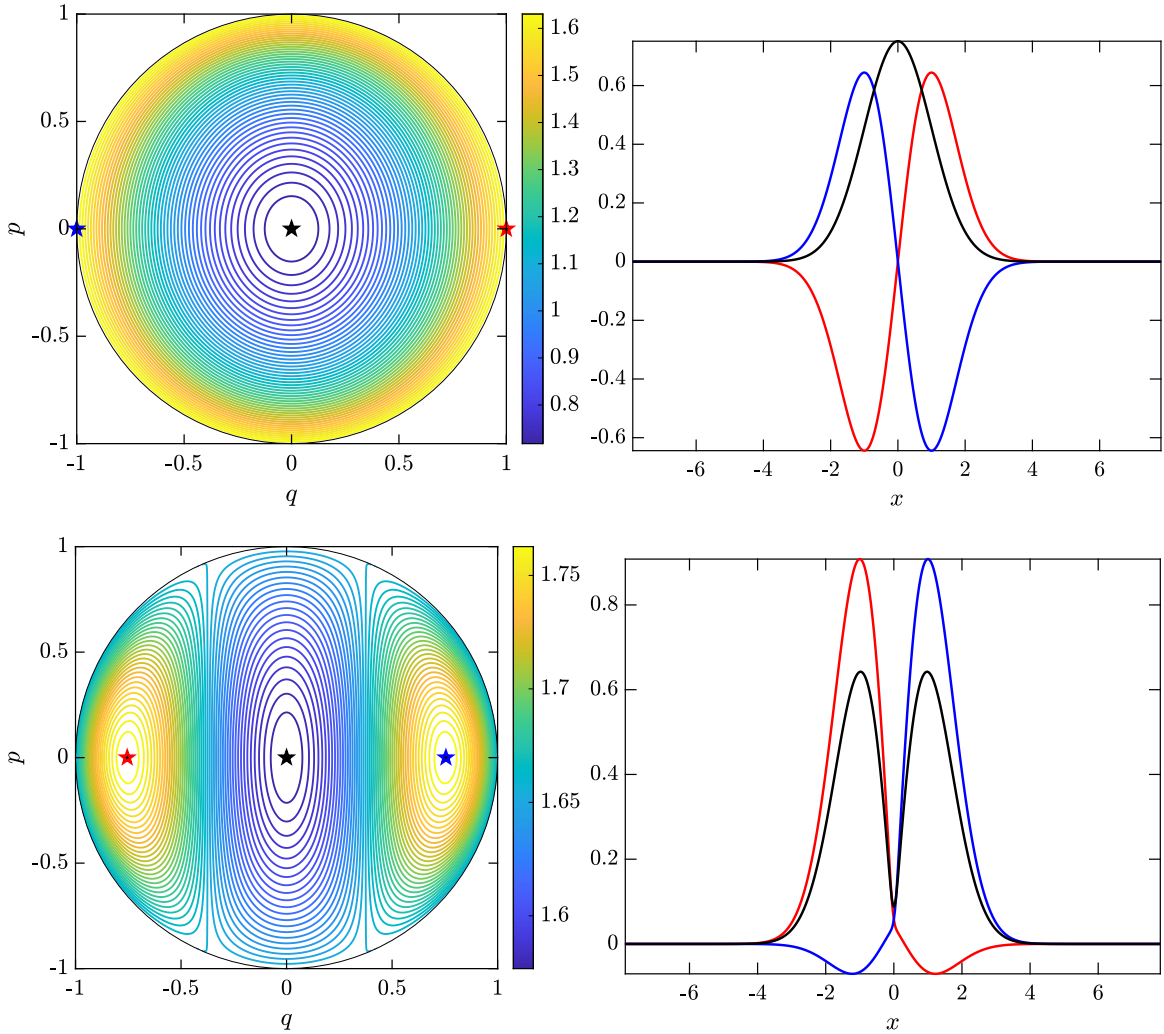


Fig. 2.1. Left panels: the phase space of system (2.11) for $v = 0$ (top) and $v = 10$ (bottom), with the ground state marked with a black star, showing that two fixed points have bifurcated from the bounding circle as v was raised, now sitting at approximately $(q, p) = (\pm 0.7550, 0)$. Right panels, same parameter values, show in black the ground state standing wave and in red/blue the odd-symmetric standing waves (top) and the symmetry broken standing waves ψ_0 and ψ_d (bottom).

(except for very low masses M_d). Of course, to find the coefficients c_0 and c_1 , we back substitute using the above canonical transformations through

$$c_0 = \sqrt{M_d - q^2 - p^2} e^{i\theta}, \quad c_1 = (q + ip) e^{i\theta}, \tag{2.12}$$

where $\theta \in [0, 2\pi]$ is arbitrary by the phase invariance of the Hamiltonian (2.11). Without loss of generality, we choose $\theta = 0$ so that ψ_2^{Gal} , given by Eq. (2.5), is real.

Hereafter, we fix the barrier height to $v = 10$, and choose the value of M_d such that the stable fixed points with $q \neq 0$ are asymmetric states, as shown in Fig. 2.1. That is, we operate within the symmetry-broken regime of the double-well potential. We note that for any finite-strength barrier, the stable state is “partially fragmented” in that a nonzero fraction of the mass resides in each well; see [37] for a theoretical account within the many-body formalism of BEC. As the value of v is further increased, the fragmentation is lessened, which provides an obvious strategy for mitigating fragmentation.

Moving forward, the phase space shown in (the bottom panels of) Fig. 2.1 makes clear the goal of our optimal control problem: to find functions $u(t)$ and $v(t)$, with fixed and identical initial and terminal conditions, that drive the system from one asymmetric steady state $\psi_0(x)$ to the other one $\psi_d(x)$. From a physical perspective, our aim is to drive atoms from a state in which most reside in one well, into one in which most reside in the other, using the experimentally-developed ability to temporally drive double-well potentials [11] and more specifically magnetic and optical confining beams [3,4,29]. This control problem is mathematically formulated in Section 3.

Numerical validation

Before describing the optimal control problem in detail, we numerically test the ability of the two-mode system (2.6) to approximate the dynamics of the GPE (2.1) with appropriate initial conditions. We consider the evolution of the initial condition $\psi(x, 0) = \varphi_0(x)$ as shown in Fig. 2.1 subject to the GPE with imposed controls

$$u_{\text{trial}}(t) = 1 + 2 \sin\left(\frac{\pi t}{T}\right) \quad \text{and} \quad v_{\text{trial}}(t) = 10 \cos^4\left(\frac{\pi t}{T}\right) \tag{2.13}$$

over the time interval $t \in [0, T]$, with $T = 2$. We have proposed these trial controls based on ad hoc reasoning, using on the following partial intuition: before performing an optimization, we suspect that an optimal potential would allow the barrier at the origin to lower so that the initial mass on the one well can be transferred significantly to the other well, followed by a raising of the barrier anew in order to localize the wavefunction into the desired well of the potential. The choices in the modulation of the parabolic trap, the strength of the localized barrier, and the length of time in the simulation were all chosen arbitrarily in this dynamical example.

It does not escape us that in physical settings involving quasi-1d double wells in atomic BECs, the width parameter u is constrained to be $u(t) \ll 1$ for the quasi-1d reduction to hold. We have considered such scenarios as well, finding qualitatively similar results, as regards the optimal control framework discussed later on in Section 3 within the Galerkin truncation, although over considerably longer time scales.

We numerically integrate the two-mode system (2.6) using MATLAB’s `ode45`. Its time-dependent coefficients from Eq. (2.7) depend on $\mathbf{w}(t)$ through the instantaneous eigenfunctions φ_0 and φ_1 . While closed form expressions for these eigenfunctions are determined, for each value of \mathbf{w} , in terms of hypergeometric functions [38], we find it simpler to solve the associated eigenproblem numerically at each time step using MATLAB’s `eig` command. Indeed, while the former possibility is particular to the potential considered herein, the latter can be extended to arbitrary time-dependent potentials.

We solve the GPE (2.1) using a second-order Fourier split-step method and approximate the delta function by a narrow Gaussian

$$\delta(x) = \lim_{a \rightarrow \infty} \frac{a}{\sqrt{\pi}} e^{-a^2 x^2}, \tag{2.14}$$

with $a = 12$ here and in all subsequent computations. Although the Fourier split-step method we use to solve the GPE is quite standard, we provide details about the method in Appendix A for completeness. Throughout this work, we find that a uniform spatial discretization on the truncated interval $x \in [-5\pi, 5\pi]$ of 2^{11} points and a temporal discretization of T/h points, choosing $h = 2^{-8}$, yields an accurate and stable computation of the GPE dynamics.

In what follows, we need a way to measure the agreement between the solutions to GPE and the finite-dimensional approximation defined by expansion (2.5). We define the projected wavefunction as

$$\psi_{N+1}^{\text{proj}} = \sum_{n=0}^N \langle \psi^{\text{GPE}}(\cdot, t), \varphi_n(\cdot, u(t)) \rangle \varphi_n(x, u(t)), \tag{2.15}$$

where ψ^{GPE} solves Eq. (2.1). We quantify an expected upper bound on the Galerkin approximation (2.5) through the relative error

$$\varepsilon_{N+1}(t) = \frac{\|\psi^{\text{GPE}} - \psi_{N+1}^{\text{proj}}\|^2}{M} = \frac{\|\sum_{n=N+1}^{\infty} \langle \psi^{\text{GPE}}(\cdot, t), \varphi_n(\cdot, \mathbf{w}(t)) \rangle \varphi_n(x, \mathbf{w}(t))\|^2}{M}, \tag{2.16}$$

where M is defined by Eq. (2.2) and the norm is taken in $L^2(\mathbb{C})$. The second equality, which is interpreted as the relative mass content which has been excited beyond the few-mode representation at order N , relies on the fact that the GPE (2.1) is well-approximated by Formula (2.15) in $L^2(\mathbb{C})$, i.e., $\varepsilon_{N+1} \rightarrow 0$ as $N \rightarrow \infty$. Therefore, we rely on various comparisons among Eqs. (2.5), (2.15), and (2.16) when discussing the extent to which few-mode representations effectively shadow the full-dynamical picture given by the GPE (2.1). Also, note that although wavefunctions are normalized to have unit mass throughout this work, we include M in the above definition of ε_{N+1} to maintain clarity of how the analysis should be performed given a different scaling of Eq. (2.1).

With those preliminaries, we are ready to show the results of the simulations. Fig. 2.2 shows simulations the GPE (2.1) and the two-mode model system (2.6). It presents three colormaps: the wave function ψ^{GPE} , the projection of the wave function onto the first two instantaneous eigenfunctions, i.e., ψ_2^{Gal} , and the wave function ψ_{N+1}^{Gal} constructed from the solution to the two-mode model (2.6) using Formula (2.5). A fourth plot shows the solutions of Eq. (2.6) as well as the coefficients defining the projected wavefunction (2.15) from the GPE solution.

We make two observations based on these plots. First, our naively chosen control functions (2.13) crudely transfer the bulk of the solution from the left potential well to the right, in both the GPE system and the two-mode model system. Second, and despite the first observation, the agreement between the two dynamics is poor. This is seen in the poor agreement to the computed values of the coefficients and through the large relative error $\varepsilon_2(t)$.

This is a central observation of this study: while the two-mode reduction effectively describes the bifurcation structure and the dynamical evolution in the vicinity of the symmetric and asymmetric equilibrium. However, for the more highly non-equilibrium transfer proposed herein, a representation requiring more modes becomes necessary. In that light, we now pursue a three-mode reduction of the system.

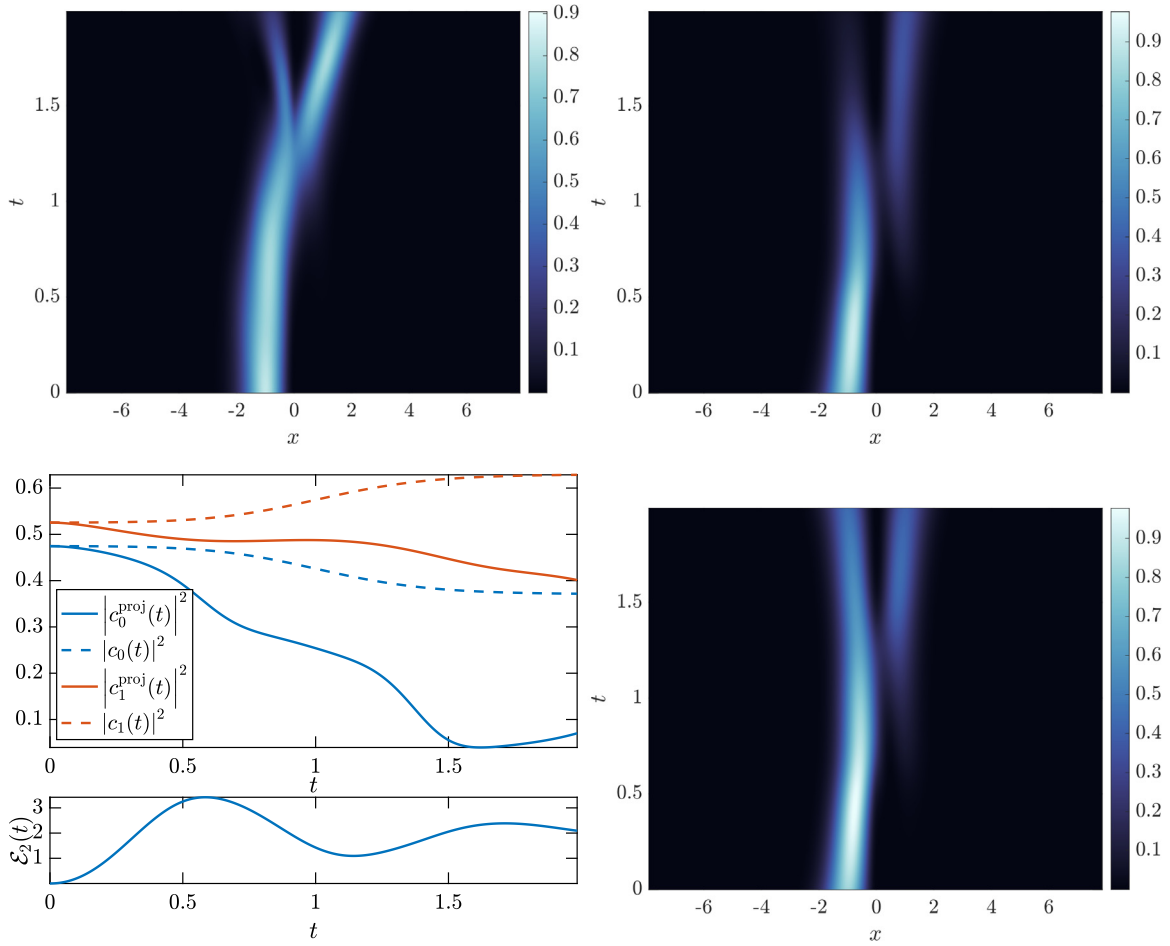


Fig. 2.2. A comparison between numerical solutions to the GPE (2.1) and the two-mode system given by Eqs. (2.6). Top left: a full numerical simulation of the GPE (2.1) with the colormap showing the squared amplitude. Top right: the projected wavefunction ψ_2^{proj} , in absolute value squared, as in Eq. (2.15). Bottom left: a comparison of numerically computed and projected coefficients $c_n(t)$ for $n = 0$ and $n = 1$, as well as the loss of mass to higher modes given by the error formula (2.16). Bottom right: the wavefunction ψ_2^{Gal} , as defined by Eq. (2.5) and also in absolute value squared, with coefficients shown in the bottom left panel.

2.2. Three-mode expansion

In order to increase the fidelity of the reduced model to the full GPE, we now compute a model equation using $N = 2$ in the expansion (2.5). The form of the Hamiltonian system is long and fairly unenlightening, so we display the associated Hamiltonian (B.1) in Appendix B. To simplify the search for stationary solutions, we perform a canonical transformation similar to Eq. (2.12), yielding Hamiltonian (B.6). Not surprisingly, we find asymmetric standing waves similar to ψ_0 and ψ_d from Fig. 2.1. In fact, the contribution to these modes from c_2 is no greater than one part in 10^{-10} in absolute-value squared. This numerically justifies the simplification of using the fixed point, corresponding to the left-asymmetric state from Fig. 2.1, with no contribution from the third mode. Additionally, this also allows for consistency in testing the accuracy of the three-mode model.

Using the above-mentioned initial condition, we run the same test shown in Fig. 2.2, but for the three-mode model, as shown in Fig. 2.3. In this case, the approximation is considerably more accurate, especially up to intermediate times. For example at $t = 1$, the relative error ϵ_3 is about 0.05. More importantly, we see that the even modes in the reduction effectively capture the even-projected dynamics of the GPE (2.1) for up to intermediate times.

However, we lose a great deal of accuracy for the remainder of the simulation, where, by $t = T$ the relative error has grown to about 0.40. The plot of c_1 and c_1^{proj} shows that this is due to a significant excitation of higher-order odd modes which have been neglected. Despite this, we find that the three-mode model performs well enough in our pursuit of optimal controls. In Section 4, we quantify the contribution of the higher modes to the relative error (2.16) while the condensate is being controlled in the full dynamical setting. We find that the inclusion of just one more odd

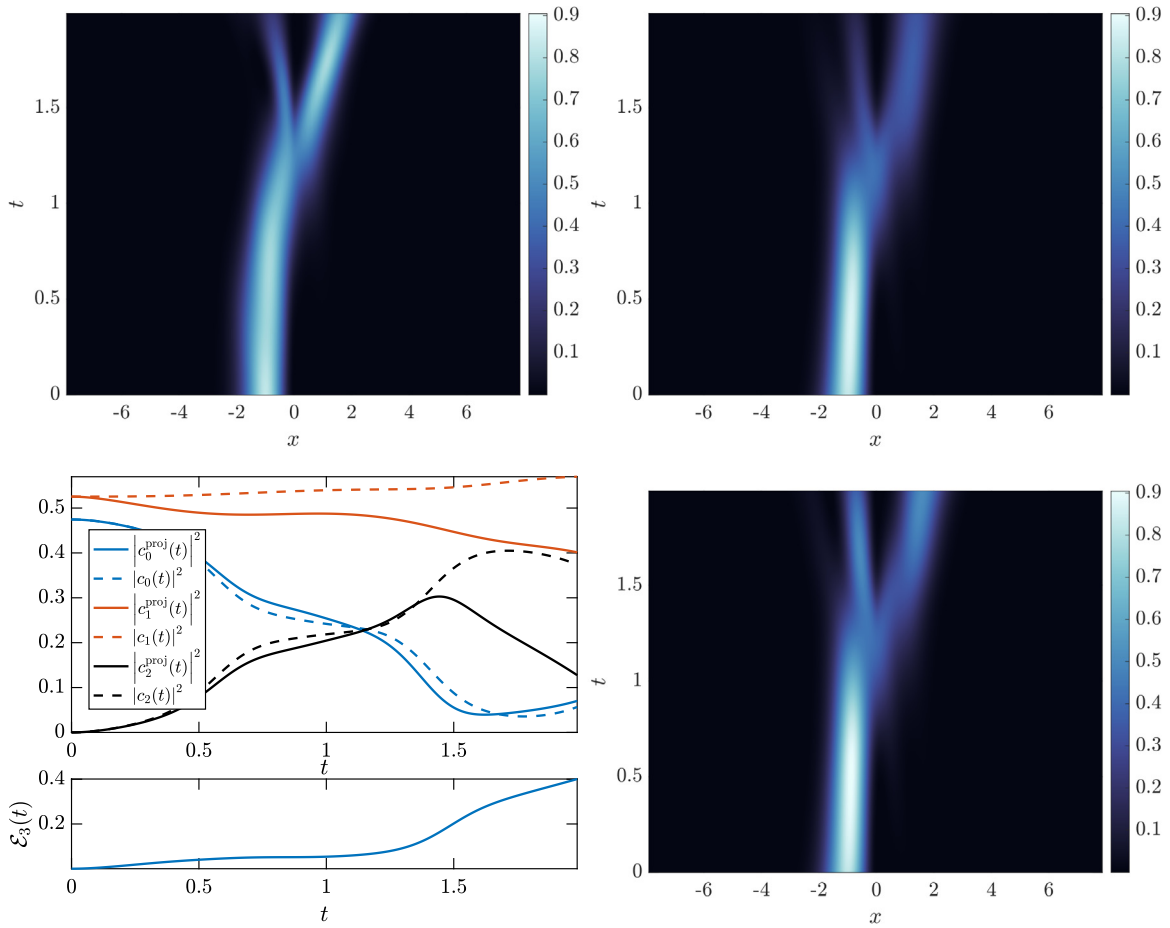


Fig. 2.3. A comparison between numerical solutions to the GPE (2.1) and the three-mode system given by Hamiltonian (B.1) as was similarly presented in Fig. 2.2. Here, we see a substantial reduction in the error $\varepsilon_3(t)$ in contrast with the error $\varepsilon_2(t)$ shown in Fig. 2.2, allowing the three-mode model to more effectively capture the full dynamics given by Eq. (2.1).

mode substantially reduces the relative error. There, we discuss this in greater detail, and, for now, leave the pursuit of higher-dimensional models as a subject for future work.

We make a final comment on the role that the mass M has on the relative error ε_3 . Indeed, for smaller values of the mass M , we see a reduction in ε_3 , as expected since nonlinear interactions in Eq. (2.1) are substantially smaller. Using $M = 0.2$ which is only slightly above the symmetry-breaking bifurcation value, we find $\varepsilon(T)$ to be near 0.25. Although this error has been reduced, enhancing the efficacy of the reduced dynamical system, the mode ψ_0 corresponding to the asymmetric stationary state of Hamiltonian (2.11) is only slightly asymmetric, failing to meet our stated goal of concentrating the mass in a single well. For this reason, we continue to use $M = 1$ in what follows, since this strikes a good balance between a small enough relative error and an adequate initial condition ψ_0 .

3. Optimal control strategy

The optimal control problem we pursue, motivated by the previous section, is to construct a function $\mathbf{w}(t)$ that drives an initial state \mathbf{c}_0 to the desired state \mathbf{c}_d under the dynamics of the two- or three-mode model. More precisely, the control problem is to find a local minimizer of the problem

$$\min_{\mathbf{w}(t) \in \mathcal{W}} \mathcal{J} = \min_{\mathbf{w} \in \mathcal{W}} \{M_d^2 - |\langle \mathbf{c}_d, \mathbf{c}_T \rangle|^2\}, \tag{3.1}$$

where the admissible space of controls is given by $\mathcal{W} = \{\mathbf{w}(t) \in C^0([0, T]) : \mathbf{w}(0) = \mathbf{w}(T) = \mathbf{w}_b\}$, for a prescribed value of \mathbf{w}_b . We call this objective functional the discrete infidelity, as opposed to the full infidelity

$$\mathcal{J}_{\text{full}} = M^2 - |\langle \psi_d, \psi_T \rangle|^2 \tag{3.2}$$

first used by Hohenester, et al. [29]. In both cases, the infidelity penalizes misalignments of the final computed state with the desired state. Note that since the discrete mass M_d is conserved by the dynamics governing \mathbf{c} , the optimal, perhaps unachievable, final state is the desired, which yields an optimal infidelity of zero.

An advantage of the infidelity (3.1) is that it is insensitive to the global phase of the dynamics, which is physically unimportant. A more traditional least-squares approach can be introduced via the objective

$$\mathcal{J}_d^{\text{LSQ}} = \frac{1}{M_d} |\mathbf{c}_d - e^{iS} \mathbf{c}_T|^2, \tag{3.3}$$

where the phase $S \in [0, 2\pi]$. Although we do not pursue such an optimization we report the values of both $\mathcal{J}_d^{\text{LSQ}}$ and the value of

$$\mathcal{J}_{\text{full}}^{\text{LSQ}} = \frac{1}{M} \|\psi_d - e^{iS} \psi_T\|^2, \tag{3.4}$$

after a minimization over S , as a relative, and more familiar, measure of optimality at the level of the full-dynamical picture.

The optimal control problem (3.1) is posed over the admissible space \mathcal{W} , which is infinite-dimensional. We approximate this by a finite-dimensional admissible space, constructed using a Galerkin-type method called the chopped random basis method (CRAB), first used by [39,40] and explained in great detail in the work of [33]. We use the following basis and trial functions

$$\mathbf{w}_{\text{CRAB}} = \mathbf{w}_{\text{trial}} + \mathbf{w}_b \sum_{j=1}^{N_D} \frac{\epsilon_j^w}{j^2} \sin\left(\frac{j\pi t}{T}\right), \tag{3.5}$$

where the value of \mathbf{w}_b is consistent with the boundary conditions implied by the trial controls u_{trial} and v_{trial} in Eq. (2.13).

The amplitudes ϵ_j^w are random variables drawn uniformly from $[-1, 1]$. We choose the coefficients $A_j = j^{-2} \epsilon_j^w$ to decay quadratically because the Fourier series of absolutely continuous functions exhibit the same type of decay [41]. In this way, the search space for optimal control \mathbf{w} is not severely restricted, yet candidate controls remain technically feasible. To find the coefficients ϵ_j^w , we use the differential evolution (DE) method [42] outlined in Appendix C.

Remark. The numerical optimization problem associated with the objective functional in Eq. (3.1) is often stated in the variational form of Euler–Lagrange equations and solved using a form of gradient descent [33,43]. This requires functional derivatives of the objective \mathcal{J} with respect to the control vector \mathbf{w} and thus involves derivatives of the basis functions φ_n in Eq. (2.5). Since these derivatives cannot be written in closed form, this renders gradient-based methods cumbersome. Thus we choose not to pursue such a strategy here. In previous work [33], we numerically solve a similar optimization problem using both the CRAB method, and when possible, a combination of the CRAB method and gradient descent and find that the CRAB method alone is fairly successful in finding efficient control policies.

4. Results of numerical optimization

In this section, we present the results of our numerical optimization. We briefly summarize the strategy outlined over the past sections. We perform the optimization on the three-mode reduced system described by the Hamiltonian (B.1). We use the initial and desired profiles for the two-mode system shown in Fig. 2.1, as we found that c_2 was negligibly small in the corresponding stationary solutions of the three-mode system. We minimize the phase-insensitive infidelity \mathcal{J} defined in Eq. (3.1). The control function $\mathbf{w}(t)$ is constructed using the CRAB method (3.5), and the optimization is performed using the DE method described in Appendix C. We find, through trial and error, that $N_D = 15$ basis functions are sufficient for the CRAB approximation. That is, a CRAB basis (3.5) with this many modes reduces the optimal control problem (3.1) to a nonlinear programming problem in $2N_D$ dimensions whose solution we find acceptable.

Fig. 4.1 shows the result of this numerical optimization. This computation yielded an objective function $\mathcal{J} = 0.0501$, as defined by Eq. (3.1), and a least squares infidelity $\mathcal{J}_{\text{LSQ}} = 0.0422$, as defined by Eq. (3.3). The figure also shows the full infidelity $\mathcal{J}_{\text{full}}$ and the full least-squares objective $\mathcal{J}_{\text{full}}^{\text{LSQ}}$ resulting from using optimal controls in simulating the GPE (2.1).

It is important to recognize that the dynamics selected by the optimizer somewhat conforms to the anticipated physical intuition about the optimal strategy. It can indeed be observed in the figure that the barrier height $v(t)$ decreases to about 0, while the parabolic confinement becomes tighter, which enables the mass to be transferred from one side of the lowered barrier to the other. This transfer is visible at time $t \approx 1$ in the top right panel of the figure. Subsequently, $v(t)$ rises sharply again, as the parabolic confinement returns to its original value, so that the combination of the two now ensures confinement of the transmitted mass to the right well. It is through this procedure that the infidelity is substantially decreased in the lower left panel, and indeed subsequently remains small, during the return of the confinement conditions to their original settings.

We also show, in Fig. 4.2, an error analysis. The left panel in Fig. 4.2 is equivalent to the lower-left panel of Fig. 2.3, showing the coefficients $c_j(t)$ and the relative error $\epsilon_3(t)$ defined by Eq. (2.16). While the $\max_t \epsilon_3(t)$ is lower in the simulation using the optimal control, than in the trial control, it is interesting to note that using the optimal control yields significantly better agreement between the dynamics of the full GPE system and its projection onto the first three

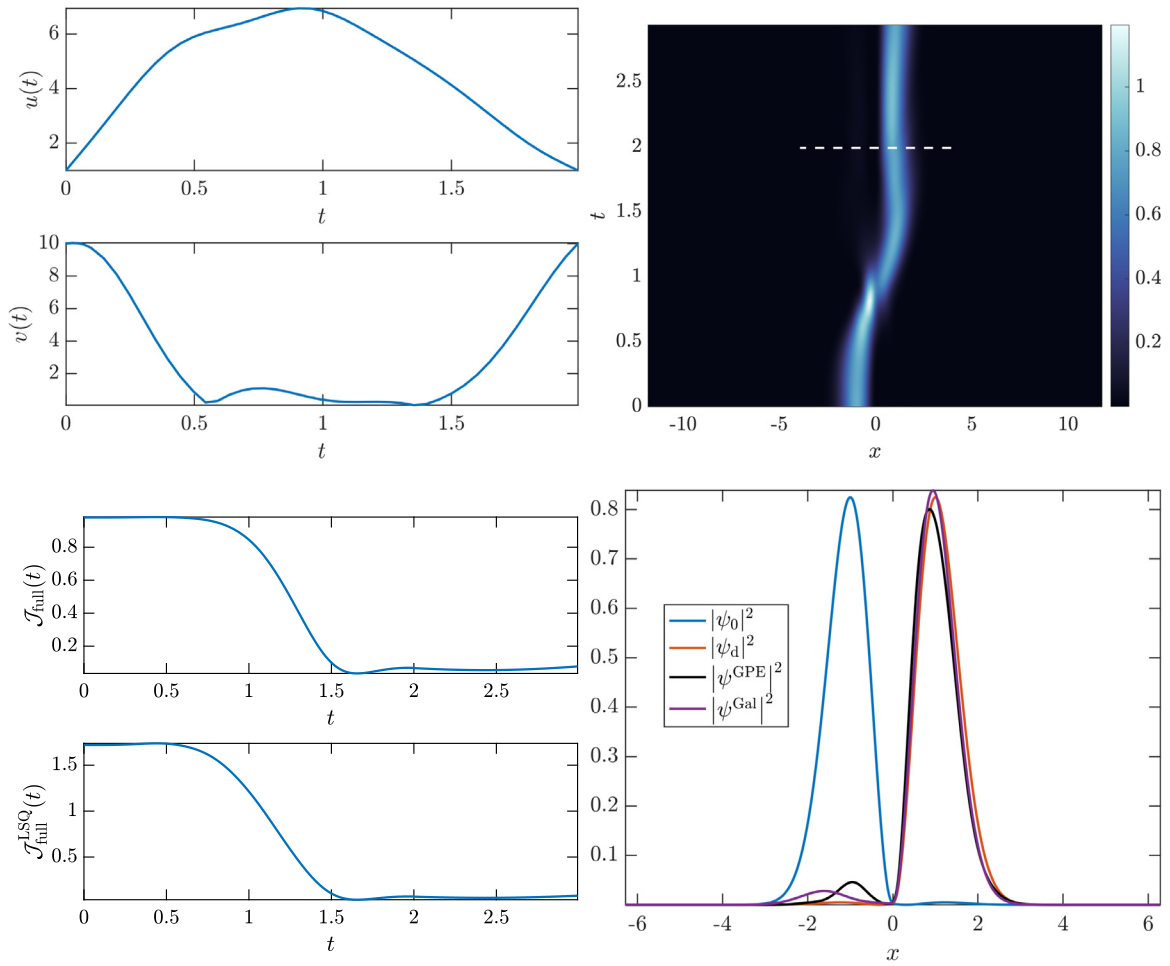


Fig. 4.1. The result of using numerical optimal control theory. Top left: optimal controls identified via our numerical methodology. Top right: The solution of the GPE (2.1) in absolute-value squared. The dotted white line, at $T = 2$, represents the moment the controls are held at their constant terminal values \mathbf{w}_b . Bottom left: the full infidelity $\mathcal{J}_{\text{full}}$ and full modified least-squares objective $\mathcal{J}_{\text{full}}^{\text{LSQ}}$. Bottom right: wavefunction profiles, in absolute-value squared, of the initial state ψ_0 , the desired state ψ_d the state ψ^{Gal} computed via the three-mode model at $T = 2$, and the state ψ^{GPE} computed via the GPE (2.1) at $T = 2$.

modes at the final time T , decreasing from a maximum of about 18% to just about 5% at time T . The right panel of the figure computes the error $\mathcal{E}_N(t)$ for values of $N \leq 6$. We find $\mathcal{E}_N(t)$ decreases monotonically, pointwise in t , as expected. Although we have shown that three modes suffice to control the GPE, this result indicates the expected accuracy for $N > 3$.

5. Conclusions

In the present work, we have applied the methodology of optimal control to dynamics in double-well potentials, one of the most prototypical (and highly controlled) experimental settings, both in atomic Bose-Einstein condensates and in nonlinear optics. We have used a finite-dimensional model derived via Galerkin truncation to reduce the dimensionality of the optimal control calculation and to gain insight into its behavior. Typically, two-mode truncations are used to explore the steady states, stability, bifurcations, and dynamics of such double-well systems. A key finding of the present work is that such a two-mode approximation is not sufficient to characterize the dynamics associated with optimal transport.

Indeed, it was found that a *three-mode* approximation was crucial in order to describe the relevant dynamical process, identified as optimal by the differential evolution algorithm. Despite quantitative inaccuracies in using a low-order Galerkin reduction, we see that controlling the three-mode model effectively controls the GPE wavefunction in numerical simulations. Furthermore, our numerical results showcase the extent to which the model can be refined by including more modes in the Galerkin reduction—recalling that the chosen basis is L^2 -complete so that the Galerkin representation converges to the wavefunction ψ satisfying the GPE in L^2 as the number of modes N increases. In particular, our

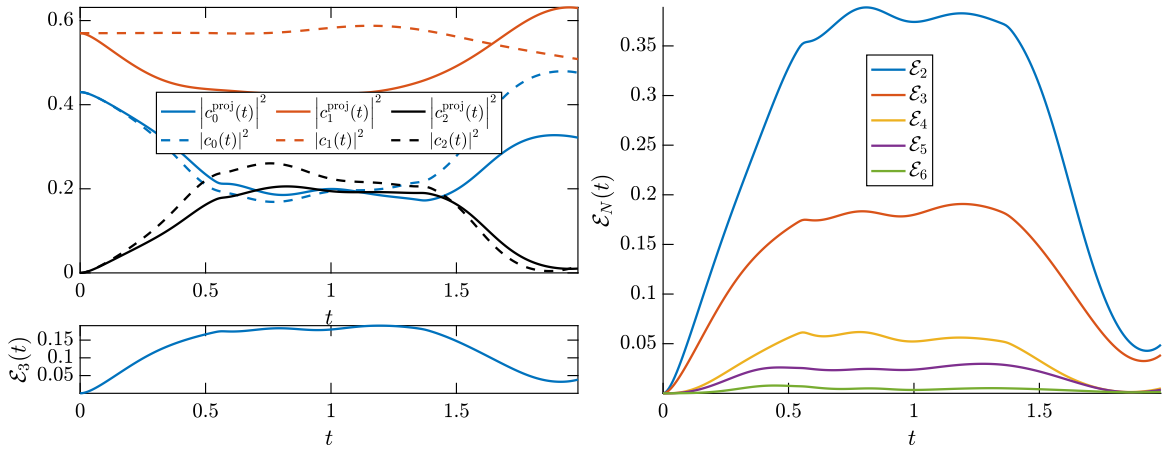


Fig. 4.2. Left: Numerical solution of the three-mode model, projected coefficients, and the error consistent with Fig. 4.1. Right: the error of modes two through six, with the natural number N used consistently with the Galerkin reduction defined by Eq. (2.5).

computations, shown in Fig. 4.2, indicate that including a fourth mode in the model could lead to substantial gain. We leave the potential inclusion of these higher modes in a reduction-based optimal control strategy as a subject for future work.

Additionally, using Galerkin reductions as part of the optimal control process could be useful in additional applications. Some possibilities include multi-component and spinor condensates [44] where few-mode approximations have proven useful [21–23]. Moreover, extending such control strategies beyond the mean-field framework and into the realm of many-body effects [24,25], is of particular interest in its own right; for a review of the latter, see, e.g., the recent preprint of [45]. In regards to complementary or alternative low-dimensional control strategies, it should be possible to couple the optimal control methods used here with methods based on the so-called shortcut to adiabaticity [46]. We additionally note that other methods more tailored to the driving of specific potentials [47], as well as ones that are model agnostic [48] also exist in the literature and are of interest in their own right.

It is also natural to extend these ideas to higher-dimensional systems where few-well arrangements have also been explored [26] or to systems with disorder, such as recent work which makes use of deep learning [49]. The Galerkin approach here may be generalized to systems with disorder so that optimal control policies can be computed via a low-dimensional dynamic program. Such studies are currently under consideration and will be presented in future publications.

CRediT authorship contribution statement

Jimmie Adriazola: Methodology, Software, Writing – original draft. **Roy Goodman:** Methodology, Supervision, Writing – review & editing. **Panayotis Kevrekidis:** Conceptualization, Supervision, Writing – review & editing.

Declaration of competing interest

The authors declare that they have no known competing financial interests or personal relationships that could have appeared to influence the work reported in this paper.

Data availability

Data will be made available on request.

Acknowledgments

This material is based upon work supported by the US National Science Foundation under Grants No. DMS-1809074 and PHY-2110030 (P.G.K.).

Appendix A. Numerical method for solving the Gross–Pitaevskii equation

It is necessary to solve the GPE (2.1) in order to validate the Galerkin reduction (2.5) and to evaluate the performance of the dimensionally reduced optimal control problem. The boundary conditions are assumed to be periodic so that the use of spectral methods is straightforward. We use an operator splitting method, and, to this end, rewrite Eq. (2.1) in the form

$$i\partial_t \psi = \mathcal{L}\psi + \mathcal{N}(\psi), \quad (\text{A.1})$$

where the linear operator is given by $\mathcal{L} = -\frac{1}{2}\partial_x^2$ and the nonlinear and inhomogeneous operator $\mathcal{N}(\psi)$ incorporates the remaining terms.

We choose to use a second order in time operator splitting, often referred to as Strang splitting [50], to approximate the resulting matrix exponential by

$$e^{(\mathcal{L}+\mathcal{N})Mh} = e^{\mathcal{L}h/2} e^{\mathcal{N}h} e^{\mathcal{L}h} \dots e^{\mathcal{L}h} e^{\mathcal{N}h} e^{\mathcal{L}h/2} + \mathcal{O}(h^2), \quad (\text{A.2})$$

where $h = T/M$ is the time discretization for a given number of time steps M . The solution of the linear equation resulting from the matrix exponential $e^{\mathcal{L}h}$ is facilitated by the Fourier transform and is given by

$$\psi_{n+1} = \mathcal{F}^{-1} \left\{ \mathcal{F}\{\psi_n\} e^{-\frac{ihk^2}{2}} \right\}, \quad (\text{A.3})$$

where \mathcal{F} and \mathcal{F}^{-1} denote the Fourier and inverse Fourier transformation, respectively. Fourier and inverse Fourier transforms are computed via the fast Fourier transform functions in MATLAB, `fft` and `ifft`, with discretized wavenumbers $k \in \left[\frac{-N/2+1}{2l}, \frac{N/2-1}{2l} \right]$, where $2\pi l$ units of length are assumed in the truncated spatial domain and N is the number of spatial discretization points.

The nonlinear equation resulting from the matrix exponential $e^{\mathcal{N}h}$ is quite simple. Since the nonlinearity does not involve spatial derivatives, we are simply tasked with solving ODEs. Using polar coordinates, i.e., letting

$$\psi = \rho(x, t) e^{i\theta(x, t)}, \quad (\text{A.4})$$

results in the system

$$\begin{aligned} \partial_t \rho &= 0, \\ \partial_t \theta &= -\rho^2 - V(x, t). \end{aligned} \quad (\text{A.5})$$

The first of these equations is a statement about conservation of the mass $\|\psi\|_{L^2(\mathbb{C})}$. The second equation, governing the phase θ , can be solved via any number of standard numerical ODE techniques; we simply use the second-order accurate midpoint method. The update for the phase θ , in this case, is

$$\theta(x, t_{n+1}) = \theta(x, t_n) - h\rho(x, t_n)^2 - hV\left(x, t_n + \frac{h}{2}\right) \quad (\text{A.6})$$

Appendix B. Details of the three-mode model

The Hamiltonian for the three-mode model is found to be

$$\mathcal{H} = \alpha|c_0|^2 + \beta|c_1|^2 + \sigma|c_2|^2 + 2\Delta \text{Im}\{c_0\bar{c}_2\} + \frac{\gamma_0}{2}|c_0|^4 + \frac{\gamma_1}{2}|c_1|^4 + \frac{\gamma_2}{2}|c_2|^4 \quad (\text{B.1})$$

$$\begin{aligned} &+ \gamma_3 (\Re\{c_0^2\bar{c}_1^2\} + 2|c_0|^2|c_1|^2) + \gamma_4 (\Re\{c_0^2\bar{c}_2^2\} + 2|c_0|^2|c_2|^2) + \gamma_5 (\Re\{c_1^2\bar{c}_2^2\} + 2|c_1|^2|c_2|^2) \\ &+ 2(\gamma_6|c_0|^2 + \gamma_7|c_2|^2) \Re\{c_0\bar{c}_2\} + 2\gamma_8 (\Re\{c_0\bar{c}_1^2c_2\} + 2\Re\{c_0|c_1|^2\bar{c}_2\}), \end{aligned} \quad (\text{B.2})$$

where the projection coefficients are given by

$$\begin{aligned} \alpha &= \langle \mathcal{L}\varphi_0, \varphi_0 \rangle, \quad \beta = \langle \mathcal{L}\varphi_1, \varphi_1 \rangle, \quad \sigma = \langle \mathcal{L}\varphi_2, \varphi_2 \rangle, \quad \Delta = \langle \varphi_0, \dot{\varphi}_2 \rangle, \\ \gamma_0 &= \|\varphi_0^4\|, \quad \gamma_1 = \|\varphi_1^4\|, \quad \gamma_2 = \|\varphi_2^4\|, \quad \gamma_3 = \langle \varphi_0^2, \varphi_1^2 \rangle, \quad \gamma_4 = \langle \varphi_0^2, \varphi_2^2 \rangle, \\ \gamma_5 &= \langle \varphi_1^2, \varphi_2^2 \rangle, \quad \gamma_6 = \langle \varphi_0^3, \varphi_2 \rangle, \quad \gamma_7 = \langle \varphi_0, \varphi_2^3 \rangle, \quad \gamma_8 = \langle \varphi_0, \varphi_1^2 \varphi_2 \rangle. \end{aligned} \quad (\text{B.3})$$

from which the analogous system to the two-mode system (2.6) can be derived easily. The appearance of the term with coefficient Δ is due to the time-dependent nature of the basis functions φ_n , and did not appear in the two-mode system due to the parity of the first two modes. This, as well as the implicit claim that $\langle \varphi_0, \dot{\varphi}_2 \rangle = -\langle \varphi_2, \dot{\varphi}_0 \rangle$ may be verified numerically.

As was done with the two-mode system, we use changes of variables and the, now three-mode, discrete mass to reduce dimensionality. Because we may only reduce the number of degrees of freedom to two for the three-mode system, we

lose the comfort of visualizing the dynamics via phase portraits as before. Nevertheless, we pursue a reduction since this helps make identifying fixed points of the dynamical system simpler. To this end, we begin by using

$$c_0 = \eta_0 e^{i\theta}, \quad c_1 = r e^{i\theta}, \quad c_2 = \eta_1 e^{i\theta}, \quad (\text{B.4})$$

where $\eta_j \in \mathbb{C}$ and $r \in \mathbb{R}$. We can easily eliminate r by using the discrete mass once again: $r = \sqrt{M_d - |\eta_0|^2 - |\eta_1|^2}$. Now, converting to polar coordinates via

$$\eta_0 = \sqrt{\rho_0} e^{i\theta_0}, \quad \eta_1 = \sqrt{\rho_1} e^{i\theta_1}, \quad (\text{B.5})$$

we find the following, two-degree of freedom Hamiltonian

$$\begin{aligned} \mathcal{H} = & \frac{M_d}{2} (2\beta + \gamma_1 M_d) + \frac{\rho_0^2}{2} (\gamma_0 + \gamma_1 - 2\gamma_5 (\cos(2\theta_0) - 2)) - \frac{\rho_1^2}{2} (\gamma_1 + \gamma_2 - 2\gamma_7 (\cos(2\theta_1) - 2)) \\ & \rho_0 (\alpha - \beta - \gamma_1 M_d + \gamma_5 M_d (2 + \cos(2\theta_0))) + \rho_1 (\beta + \gamma_1 M_d - \gamma_7 M_d (2 + \cos(2\theta_1)) - \sigma) \\ & + \rho_0 \rho_1 (\gamma_1 - \gamma_5 (2 + \cos(2\theta_0)) + \gamma_6 (2 + \cos(2(\theta_0 - \theta_1))) - \gamma_7 (2 + \cos(2\theta_1))) \\ & + 2\rho_0^{3/2} \rho_1^{1/2} (\gamma_3 \sin(\theta_0) \sin(\theta_1) - \gamma_8 \sin(\theta_0) \sin(\theta_1) + \gamma_3 \cos(\theta_0) \cos(\theta_1) - 3\gamma_8 \cos(\theta_0) \cos(\theta_1)) \\ & + 2\rho_0^{1/2} \rho_1^{3/2} (\gamma_4 \sin(\theta_0) \sin(\theta_1) - \gamma_8 \sin(\theta_0) \sin(\theta_1) + \gamma_4 \cos(\theta_0) \cos(\theta_1) - 3\gamma_8 \cos(\theta_0) \cos(\theta_1)) \\ & + 2M_d \gamma_8 \sqrt{\rho_0 \rho_1} (\sin(\theta_0) \sin(\theta_1) + 3 \cos(\theta_0) \cos(\theta_1)). \end{aligned} \quad (\text{B.6})$$

Appendix C. Optimization via differential evolution

DE is a stochastic optimization method used to search for candidate solutions to non-convex optimization problems. The idea behind DE is a so-called genetic algorithm that draws inspiration from evolutionary genetics. DE searches the space of candidate solutions by initializing a population set of vectors, known as agents, within some chosen region of the search space. These vectors are then randomly mutated into a new population set, or generation.

Algorithm 1: Differential Evolution Mutation

Result: A vector z mutated from agents in a given generation as required by the DE Algorithm (2).
Input: 4 distinct members a, b, c, d from the current generation of agents each with N components, the crossover ratio $R_C \in (0, 1)$, and weight $F \in (0, 2)$.

```

for  $j=1:N$  do
    Compute a random variable  $\text{rand}$ ;
    if  $\text{rand} < R_C$  then
        |  $z[j] \leftarrow a[j] + F * (b[j] - c[j])$ 
    else
        |  $z[j] \leftarrow d[j]$ 
    end
end
    
```

Algorithm 2: Differential Evolution

Result: A vector likely to be globally optimal with respect to an objective J .
Input: A maximum number of iterations N_{\max} , crossover ratio $R_C \in (0, 1)$ and weight $F \in (0, 2)$

```

while  $\text{counter} < N_{\max}$  do
    Generate a population  $\text{pop}$  of  $N_{\text{pop}}$  vectors.
    for  $i = 1 : N_{\text{pop}}$  do
         $\text{CurrentMember} \leftarrow \text{Pop}_i$ ;
        Choose three distinct vectors  $a_i, b_i, c_i$  different from the vector  $\text{Pop}_i$ ;
        Mutate  $a_i, b_i, c_i$ , and the  $\text{CurrentMember}$  into the mutated vector  $z$  using the mutation parameters  $R_C, F$  and Algorithm 1;
        if  $J(z) < J(\text{CurrentMember})$  then
            |  $\text{TemporaryPop}_i = z$ ;
        end
    end
     $\text{Pop} \leftarrow \text{TemporaryPop}$ ;
     $\text{counter} \leftarrow \text{counter} + 1$ ;
end
    
```

The mutation operates via two mechanisms: a weighted combination and a “crossover” which randomly exchanges “traits”, or vector elements, between agents. The method requires three parameters; the weight $F \in (0, 2)$, the crossover

parameter $R_C \in (0, 1)$, and the size of the population N_{pop} , which, by Algorithm 1, is required to be an integer greater than three. A pseudo-code illustrating the implementation of the relevant algorithms is given in Algorithms 1 and 2. Through trial and error, we find the parameters $F = 0.8$, $R_C = 0.9$, $N_{\text{pop}} = 20$ work well. DE ensures that the objective functional \mathcal{J} decreases monotonically with each generation. As each iteration “evolves” into the next, inferior vectors “inherit” optimal traits from superior vectors via mutations. DE only allows mutations that are more optimal with respect to \mathcal{J} to pass to the next generation. After a sufficient number of iterations, the best vector in the final generation is chosen as the candidate solution most likely to be globally optimal with respect to an objective functional.

Genetic algorithms, which require very few assumptions about the objective functional, are part of a wider class of optimization methods called metaheuristics. Although metaheuristics are useful for non-convex optimization problems, they do not provide guarantees about the global optimality of candidate solutions. Since the algorithm is stopped after a finite number of iterations, different random realizations return different candidate optimizers. The results we show are the best among five different realizations.

In practice, we do not recommend taking fewer realizations since one runs the risk of computing highly sub-optimal controls, which, indeed, is a generic issue when solving non-convex optimization problems using stochastic methods. Of course, taking more realization is expensive, but we find that with the optimization and physical parameters used throughout this work, five realizations are sufficient to guarantee the discovery of, at least, a couple of optimal control policies which are extremely competitive with regards to the objective functional (3.1). From a computation of 30 realizations, about a third of the control policies are within 1% of the infidelity returned by the best control.

References

- [1] Kevrekidis P, Frantzeskakis D, Carretero-González R. The defocusing nonlinear Schrödinger equation. SIAM, Philadelphia, PA; 2015, From dark solitons to vortices and vortex rings.
- [2] Morsch O, Oberthaler M. Dynamics of Bose-Einstein condensates in optical lattices. *Rev Mod Phys* 2006;78:179–215.
- [3] Pethick CJ, Smith H. Bose-Einstein condensation in dilute gases. Cambridge: Cambridge University Press; 2003.
- [4] Pitaevskii L, Stringari S. Bose-Einstein condensation. Oxford: Oxford University Press; 2003.
- [5] Joannopoulos J, Johnson S, Winn J, Meade R. Photonic crystals: Molding the flow of light. Princeton: Princeton University Press; 2008.
- [6] Kivshar YS, Agrawal GP. Optical solitons: From fibers to photonic crystals. Academic Press; 2003, p. 1–540. <http://dx.doi.org/10.1016/B978-0-12-410590-4.X5000-1>.
- [7] Lederer F, Stegeman GI, Christodoulides DN, Assanto G, Segev M, Silberberg Y. Discrete solitons in optics. *Phys Rep* 2008;463(1):1–126. <http://dx.doi.org/10.1016/j.physrep.2008.04.004>, URL <https://www.sciencedirect.com/science/article/pii/S0370157308001257>.
- [8] Raghavan S, Smerzi A, Fantoni S, Shenoy S. Coherent oscillations between two weakly coupled Bose-Einstein condensates: Josephson effects, π oscillations, and macroscopic quantum self-trapping. *Phys Rev A* 1999;59:620–33.
- [9] Albiez M, Gati R, Fölling J, Hunsmann S, Cristiani M, Oberthaler MK. Direct observation of tunneling and nonlinear self-trapping in a single bosonic Josephson junction. *PRL* 2005;95:010402.
- [10] Zibold T, Nicklas E, Gross C, Oberthaler M. Classical bifurcation at the transition from Rabi to Josephson dynamics. *PRL* 2010;105:204101.
- [11] Stroescu I, Hume D, Oberthaler M. Dissipative double-well potential for cold atoms: Kramers rate and stochastic resonance. *PRL* 2016;117:243005.
- [12] Cambournac C, Sylvestre T, Maillotte H, Vanderlinden B, Kockaert P, Emplit P, et al. Symmetry-breaking instability of multimode vector solitons. *PRL* 2002;89:083901.
- [13] Kevrekidis PG, Chen Z, Malomed BA, Frantzeskakis DJ, Weinstein MI. Spontaneous symmetry breaking in photonic lattices : Theory and experiment. *Phys Lett A* 2005;340:275–80.
- [14] Kapitula T, Kevrekidis PG, Chen Z. Three is a crowd: Solitary waves in photorefractive media with three potential wells. *SIAM J Appl Dyn Syst* 2006;5(4):598–633.
- [15] Aschbacher WH, Fröhlich J, Graf GM, Schnee K, Troyer M. Symmetry breaking regime in the nonlinear Hartree equation. *J Math Phys* 2002;43(8):3879–91.
- [16] Jackson RK, Weinstein MI. Geometric analysis of bifurcation and symmetry breaking in a Gross-Pitaevskii equation. *J Stat Phys* 2004;116(1–4):881–905.
- [17] Kirr EW, Kevrekidis PG, Shlizerman E, Weinstein MI. Symmetry-breaking bifurcation in nonlinear Schrödinger/Gross-Pitaevskii equations. *SIAM J Math Anal* 2008;40(2).
- [18] Marzuola JL, Weinstein MI. Long time dynamics near the symmetry breaking bifurcation for nonlinear Schrödinger/Gross-Pitaevskii equations. *Discrete Contin Dyn Syst* 2010;28(4):1505–54.
- [19] Sacchetti A. Universal critical power for nonlinear Schrödinger equations with a symmetric double well potential. *PRL* 2009;103:194101.
- [20] Kirr E, Kevrekidis PG, Pelinovsky DE. Symmetry-breaking bifurcation in the nonlinear Schrödinger equation with symmetric potentials. *Comm Math Phys* 2011;308(3):795–844.
- [21] Wang C, Kevrekidis P, Whitaker N, Malomed B. Two-component nonlinear Schrödinger models with a double-well potential. *Physica D* 2008;237(22):2922–32. <http://dx.doi.org/10.1016/j.physd.2008.04.023>, URL <https://www.sciencedirect.com/science/article/pii/S0167278908001899>.
- [22] Günay M. Binary mixture of Bose-Einstein condensates in a double-well potential: Berry phase and two-mode entanglement. *Phys Rev A* 2020;101:043608.
- [23] Tuan J, Qiu H. A dynamical phase transition of binary species BECs mixtures in a double well potential. *Internat J Theoret Phys* 2017;56:321–7.
- [24] Masiello D, Reinhardt W. Symmetry-broken many-body excited states of the gaseous atomic double-well Bose-Einstein condensate. *J Phys Chem A* 2019;123:1962–7.
- [25] Mujal P, Juliá-Díaz B, Polls A. Quantum properties of a binary bosonic mixture in a double well. *Phys Rev A* 2016;93:043619.
- [26] Wang C, Theocharis G, Kevrekidis PG, Whitaker N, Law KJH, Frantzeskakis DJ, et al. Two-dimensional paradigm for symmetry breaking: The nonlinear Schrödinger equation with a four-well potential. *Phys Rev E* 2009;80:046611. <http://dx.doi.org/10.1103/PhysRevE.80.046611>, URL <https://link.aps.org/doi/10.1103/PhysRevE.80.046611>.
- [27] Kirk DE. Optimal control theory: An introduction. Courier Corporation; 2004.
- [28] Brif C, Chakrabarti R, Rabitz H. Control of quantum phenomena: Past, present and future. *New J Phys* 2010;12(7):075008.

- [29] Hohenester U, Rekdal PK, Borzi A, Schmiedmayer J. Optimal quantum control of Bose-Einstein condensates in magnetic microtraps. *Phys Rev A* 2007;75(2):023602.
- [30] Jäger G, Reich DM, Goerz MH, Koch CP, Hohenester U. Optimal quantum control of Bose-Einstein condensates in magnetic microtraps: Comparison of gradient-ascent-pulse-engineering and Krotov optimization schemes. *Phys Rev A* 2014;90:033628. <http://dx.doi.org/10.1103/PhysRevA.90.033628>, URL <https://link.aps.org/doi/10.1103/PhysRevA.90.033628>.
- [31] Hohenester U. OCTBEC—A Matlab toolbox for optimal quantum control of Bose–Einstein condensates. *Comput Phys Comm* 2014;185(1):194–216. <http://dx.doi.org/10.1016/j.cpc.2013.09.016>.
- [32] Menemann J, Matthes D, Weishaupt R, Langen T. Optimal control of Bose-Einstein condensates in three dimensions. *New J Phys* 2015;17(11):113027.
- [33] Adriaola J, Goodman RH. Reduction-based strategy for optimal control of Bose-Einstein condensates. *Phys Rev E* 2022;105:025311. <http://dx.doi.org/10.1103/PhysRevE.105.025311>, URL <https://link.aps.org/doi/10.1103/PhysRevE.105.025311>.
- [34] Goodman RH. Bifurcations of relative periodic orbits in NLS/GP with a triple-well potential. *Physica D* 2017;359:39–59.
- [35] Theocharis G, Kevrekidis PG, Frantzeskakis DJ, Schmelcher P. Symmetry breaking in symmetric and asymmetric double-well potentials. *Phys Rev E* 2006;74:056608. <http://dx.doi.org/10.1103/PhysRevE.74.056608>, URL <https://link.aps.org/doi/10.1103/PhysRevE.74.056608>.
- [36] Goodman RH, Marzuola JL, Weinstein MI. Self-trapping and Josephson tunneling solutions to the nonlinear Schrödinger / Gross-Pitaevskii equation. *Disc Cont Dyn Sys A* 2015;35:225–46, URL <http://www.aims sciences.org/journals/displayArticlesnew.jsp?paperID=10218>.
- [37] Spekkens RW, Sipe JE. Spatial fragmentation of a Bose-Einstein condensate in a double-well potential. *Phys Rev A* 1999;59:3868–77. <http://dx.doi.org/10.1103/PhysRevA.59.3868>, URL <https://link.aps.org/doi/10.1103/PhysRevA.59.3868>.
- [38] Viana-Gomes J, Peres NMR. Solution of the quantum harmonic oscillator plus a delta-function potential at the origin: The oddness of its even-parity solutions. *Eur J Phys* 2011;32(5):1377.
- [39] Caneva T, Calarco T, Montangero S. Chopped random-basis quantum optimization. *Phys Rev A* 2011;84:022326. <http://dx.doi.org/10.1103/PhysRevA.84.022326>, URL <https://link.aps.org/doi/10.1103/PhysRevA.84.022326>.
- [40] Calarco T, Hinds EA, Jaksch D, Schmiedmayer J, Cirac JI, Zoller P. Quantum gates with neutral atoms: Controlling collisional interactions in time-dependent traps. *Phys Rev A* 2000;61(2):022304.
- [41] Trefethen LN. *Spectral methods in MATLAB*. New York, NY: SIAM; 2000.
- [42] Storn R, Price K. Differential evolution—A simple and efficient heuristic for global optimization over continuous spaces. *J Global Optim* 1997;11(4):341–59.
- [43] Borzi A, Ciaramella G, Sprengel M. *Formulation and numerical solution of quantum control problems*. Philadelphia: SIAM; 2017.
- [44] Kawaguchi Y, Ueda M. Spinor Bose–Einstein condensates. *Phys Rep* 2012;520(5):253–381. <http://dx.doi.org/10.1016/j.physrep.2012.07.005>, Spinor Bose–Einstein condensates, URL <https://www.sciencedirect.com/science/article/pii/S0370157312002098>.
- [45] Mistakidis SI, Volosniev AG, Barfknecht RE, Fogarty T, Busch T, Foerster A, et al. Cold atoms in low dimensions—A laboratory for quantum dynamics. 2022. [arXiv:2202.11071](https://arxiv.org/abs/2202.11071).
- [46] Guéry-Odelin D, Ruschhaupt A, Kiely A, Torriontgui E, Martínez-Garaot S, Muga JG. Shortcuts to adiabaticity: Concepts, methods, and applications. *Rev Modern Phys* 2019;91:045001. <http://dx.doi.org/10.1103/RevModPhys.91.045001>, URL <https://link.aps.org/doi/10.1103/RevModPhys.91.045001>.
- [47] Mommers BJ, Pritchard A, Bell TA, Kohn RN, Olson SE, Baker M, et al. Atomtronic many-body transport using Husimi driving. 2021. <http://dx.doi.org/10.48550/ARXIV.2112.12408>, URL <https://arxiv.org/abs/2112.12408>.
- [48] Huang T, Ban Y, Sherman EY, Chen X. Machine-learning-assisted quantum control in a random environment. *Phys Rev A* 2022;17:024040. <http://dx.doi.org/10.1103/PhysRevApplied.17.024040>, URL <https://link.aps.org/doi/10.1103/PhysRevApplied.17.024040>.
- [49] Huang T, Ban Y, Sherman EY, Chen X. Machine-learning-assisted quantum control in a random environment. *Phys Rev Appl* 2022;17:024040. <http://dx.doi.org/10.1103/PhysRevApplied.17.024040>, URL <https://link.aps.org/doi/10.1103/PhysRevApplied.17.024040>.
- [50] Glowinski R, Osher SJ, Yin W. *Splitting methods in communication, imaging, science, and engineering*. Cham: Springer International Publishing AG; 2017, p. 95.